Electronic Supplementary Material (ESI) for Chemical Science.
This journal is © The Royal Society of Chemistry 2024

Supporting Information

In-situ Nafion-Nanofilm Oriented (002) Zn Electrodeposition for Long-Term Zinc-Ion Batteries

Da Zhang, Ziyang Song, Ling Miao, Yaokang Lv, Lihua Gan, Mingxian Liu*

D. Zhang, Dr. Z. Song, Dr. L. Miao, Prof. L. Gan, Prof. M. Liu
Shanghai Key Lab of Chemical Assessment and Sustainability, School of Chemical Science and Engineering, Tongji University, Shanghai, 200092, P. R. China.

*E-mail: liumx@tongji.edu.cn

Dr. Y. Lv
College of Chemical Engineering, Zhejiang University of Technology, Hangzhou 310014, P. R. China.

Section S1. Experimental Procedures

1.1 Preparation of Electrolyte and Cathode Materials

$Zn(OTF)_2$-H_2O Electrolyte: Different amounts of $Zn(OTF)_2$ salt were dissolved into deionized water, to obtain aqueous electrolytes with different concentrations (0.5, 1, and 2 M).

$Zn(OTF)_2$-MeOH (MeOH=methanol) Electrolyte: The preparation method is the same as that of 1 M $Zn(OTF)_2$-H_2O electrolyte, except that the water solvent is replaced with a certain amount of MeOH (V_{H_2O}: V_{MeOH} = 7 : 3).

$Zn(OTF)_2$-NAF Electrolyte: Nafion was dissolved in MeOH, and then the preparation method is the same as that of $Zn(OTF)_2$-MeOH electrolyte to obtain $Zn(OTF)_2$-NAF electrolyte (Nafion concentration:10−30 mM).

$ZnSO_4$ Electrolyte: Different amounts of $ZnSO_4$ were dissolved into deionized water, to obtain aqueous electrolytes with different concentrations (0.5, 1, and 2 M). All electrolytes mentioned above need to be stored for 24 h before use.

Manganese Dioxide Cathode Materials: In a typical synthesis, 8 mg of NaH_2PO_2-H_2O and 10 mg of $KMnO_4$ were each dissolved in 20 mL of deionized water.[1] $KMnO_4$ solution was then slowly added to NaH_2PO_4 solution by a constant pressure titration funnel under stirring for 0.5 h. The precipitate was collected after centrifugation, washed carefully with water to remove residual salt, and subsequently dried in a freeze dryer for 24 h. All chemicals were commercially available and used without any purification.

1.2 Electrode Fabrication

MnO_2 cathode was prepared by homogeneously mixing the active material (MnO_2), acetylene black and binder (polyvinylidene fluoride) with a mass ratio of 7 : 2 : 1 in *N*-methylpyrrolidone solvent. The slurry was casted onto the aluminum foil and dried at 80 °C under vacuum for 12 h to obtain MnO_2 cathode (1.5 cm^2, with a mass loading of about 2 mg cm^{-2}).

1.3 Assembly of Batteries and Electrochemical Measurements

The used battery model was standard CR2032 coin cells (MTI Corp., USA). The used anode is commercial Zn foils, and the cathodes are commercial Zn foils, Cu foils and MnO_2, respectively, for Zn||Zn, Zn||Cu and Zn||MnO_2 cells. The amount of electrolyte for all the batteries was 120 μL. The assembled battery was allowed to stand for 12 h at different temperatures (from 30 to −60 °C). The galvanostatic discharge/charge (GCD) experiments of Zn||MnO_2 batteries were carried out in the potential window of 0.9−1.9 V by LAND CT−2001A battery cycler at different current densities. The voltage window of Zn||Cu batteries was −0.5 to 2.0 V. The electrochemical impedance spectroscopy (EIS) was also carried out using the electrochemical workstation in the frequency range of 0.1 Hz to 100 kHz. The low-temperature test box was provided by Zhejiang Jiesheng Corp. (China).

1.4 Characterizations

The morphology was observed by scanning electron microscope (SEM, JEM–7900F). The transmission electron microscope (TEM) images were obtained using a JEM-F200 microscope FEI Talos F200C. X-ray photoelectron spectrometer (XPS, AXIS Ultra DLD) was utilized to investigate the surface functionalities of the samples. *In-situ* Raman measurements were performed at room temperature using a HORIBA LabRam spectrometer with a 514 nm excitation wavelength at 0.5 mW between 100 and 3,000 cm^{-1}. To avoid laser-induced deintercalation and photochemistry, the laser power was kept below 0.5 mW.[2–4] DOF polarized microscope from Olympus Corp. and Beijing Scistar Technology Co.Ltd. *In-situ* attenuated total refraction-Fourier transform infrared (ATR-FTIR) spectroscopy and scanning probe microscope (SPM) from Shimadzu Corp.

Section S2. Calculation Methods

2.1 Density Functional Theory (DFT) Calculation

First-principles calculations were performed using Gaussian 16 suite and Vienna ab initio simulation package (VASP).[5–6] The ion-electron interaction was defined using the standard projection enhanced wave method. The exchange-correlation effects were described using the fully relativistic generalized gradient approximation (GGA) proposed by Perdew-Burke-Ernzerhof (PBE).[7, 8] A energy cut-off of 400 eV and Gaussian smearing with a 0.1 eV width were used.[9] The Brillouin zone was sampled with the Monkhorst-Pack scheme at a resolution of 0.2 $Å^{-1}$.[10] To account for van der Waals interactions, the DFT-D3 correction proposed by Grimme was applied. The lattice geometries and atomic positions were fully relaxed until the atomic forces and total energy values were smaller than 0.01 eV/Å and $1.0\text{x}10^{-6}$ eV, respectively.

We simulated multiple structures at the Zn anode/electrolyte interface and calculated the single-point energies of these complexes using density functional theory (DFT) at the ωB97XD/def2–SVP level. The computational tasks were carried out using the Gaussian 6.0 package, revision A. The binding energy (ΔE) of each configuration was determined using the following equation (Eq. 1).

$$\Delta E = E_{AB} - (E_A + E_B) \qquad \text{(Eq. 1)}$$

where E_A, E_B, and E_{AB} represent the energies of A (one OTF^- or one H_2O molecule), B (excluding fragment A), and the total energy of the complex, respectively. A negative value of ΔE indicates an exothermic reaction process, and a larger negative value implies a stronger interaction, signifying greater heat release and a more stable product structure (Eq. 2).

$$E^{red} = -\frac{\Delta G^{S}298\text{K}}{F} - 0.78\ \text{V} \qquad \text{(Eq. 2)}$$

The binding energy calculation and Bader charge analysis were performed using first-principles simulations based on the DFT method with the VASP. The calculations considered projector augmented wave potentials and utilized the PBE functional within the GGA. To determine the charge transfer amount, the Bader charge analysis was conducted. Additionally, the DFT-D3 method was employed to account for long-range van der Waals interactions in the simulations.[11]

2.2 COMSOL Simulation

It is assumed that the solid electrolyte interphase (SEI) film uniformly and stably covers both the anode and cathode. To investigate Zn^{2+} transport in batteries with different electrolytes ($Zn(OTF)_2$-H_2O, $Zn(OTF)_2$-MeOH, $Zn(OTF)_2$-NAF), simulations were conducted. During the simulated deposition process, the thickness and Zn^{2+} conductivity of the SEI was kept constant.[12] By simulating the SEI at different interfaces (Zn/electrolyte and Zn/NAF/electrolyte), a comparison was made between the energy level differences and Zn^{2+} transport speeds during plating (Eq. 3).

$$\begin{cases} \vec{N}_E = -D_E \nabla c_E - nFt_E c_E \nabla \varphi_E \\ \vec{N}_S = -D_S \nabla c_S - nFt_S c_S \nabla \varphi_S \end{cases} \quad \text{(Eq. 3)}$$

The mass transfer equation (Eq. 4):

$$\frac{\partial c}{\partial t} + \nabla\ \vec{N} = 0 \quad \text{(Eq. 4)}$$

The local current density on the anode or cathode as a function of potential (φ) and Zn^{2+} concentration c can be expressed by the following equation (Eq. 5):

$$i = F\,(k_a)^{a_c}(k_c)^{a_a}\,\left(\frac{c}{c_{ref}}\right)^{a_a}\left[\,exp\left(\frac{a_a F\eta}{RT}\right) - exp\left(\frac{-a_c F\eta}{RT}\right)\right] \quad \text{(Eq. 5)}$$

where α_c and α_a are the cathodic and anodic transfer coefficients, respectively, and α_c and α_a for a single-electron reaction. H is the overpotential that can be expressed as $\eta = \varphi_{\mathrm{s}} - \Delta\varphi_{\mathrm{film}} - \varphi_{\mathrm{l}} - E_{\mathrm{eq}}$, where φ_{s} is the exerted potential on the Zn electrode, φ_{l} is the local potential, $\Delta\varphi_{\mathrm{film}}$ is the film electronic resistance and E_e is the equilibrium potential of reaction. It is noting that $\Delta\varphi_{\mathrm{film}} = \delta/\sigma_{\mathrm{SEI}}$ is only utilized in the electrolyte region to consider the SEI effect.

COMSOL Multiphysics 5.4 platform is used to establish the above model and to numerically solve it. The sizes of the simulation area are 120 μm × 25 μm for the electrolyte region, 80 nm × 15 nm for SEI of Zn anode, and 80 nm × 10 nm for SEI of Zn-NAF anode. A fine mesh was adopted with the maximum grid size of 1 μm and 1 nm for simulating the electrolyte and SEI region, respectively.

Section S3. Supporting Results

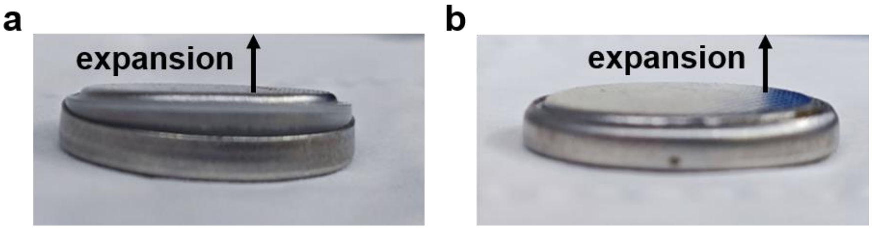

Fig. S1 The expansion of ZMBs after 500 h cycling in (a) $Zn(OTF)_2$-H_2O and (b) $Zn(OTF)_2$-NAF electrolytes.

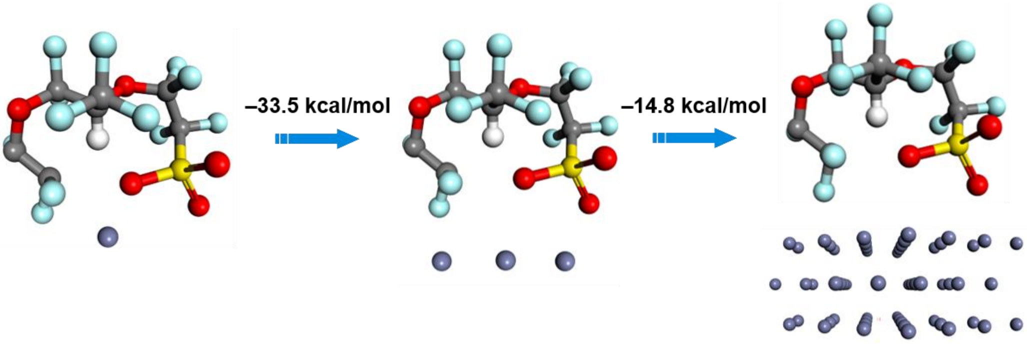

Fig. S2 Adsorption energy of Nafion molecules at the Zn interface.

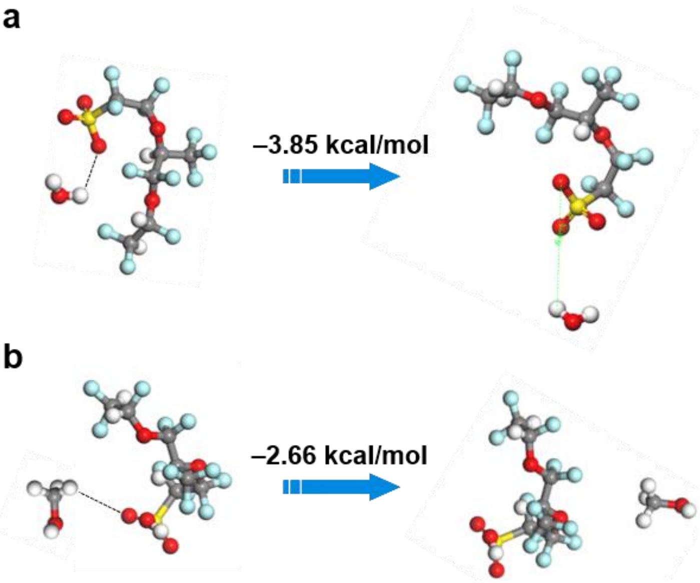

Fig. S3 Energy change of desolvation process in (a) $Zn(OTF)_2$-H_2O and (b) $Zn(OTF)_2$-NAF electrolytes.

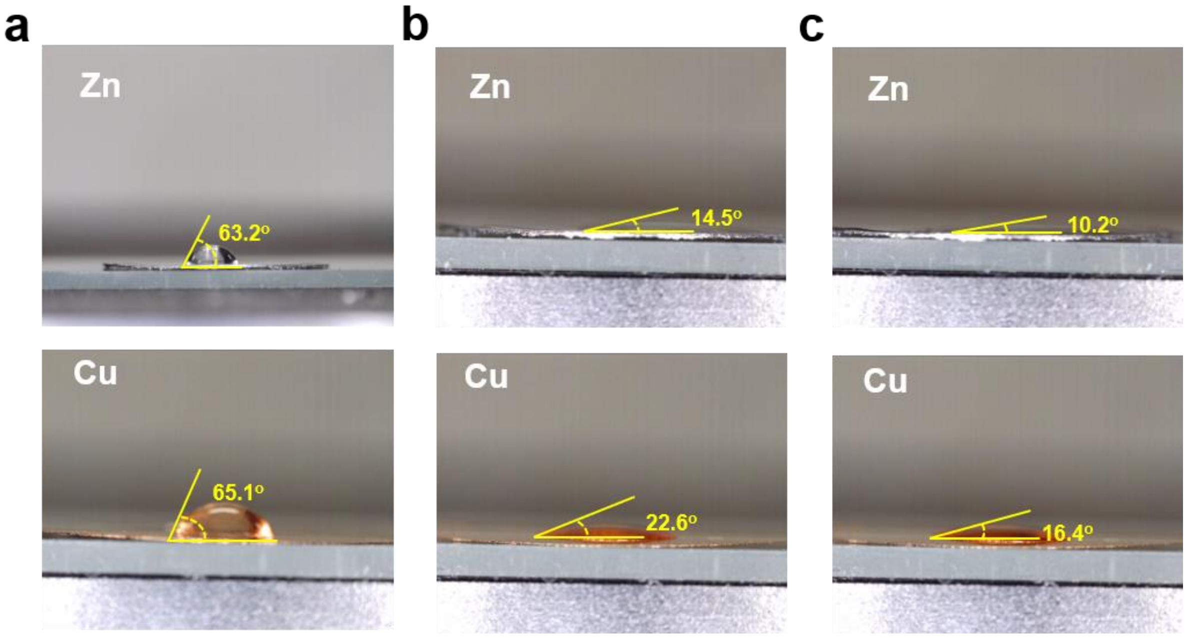

Fig. S4 Contact angles of different electrolytes on metal surfaces (Zn and Cu): (a) Zn(OTF)$_2$-H_2O, (b) Zn(OTF)$_2$-MeOH, and (c) Zn(OTF)$_2$-NAF electrolytes.

Table S1 Binding energy values of each component in different electrolytes.

Electrolyte	Zn(OTF)$_2$-H_2O	Zn(OTF)$_2$-NAF	Zn(OTF)$_2$-NAF-H_2O
Energy (Ha)	−76.4	−2239.8	−2316.2
Electrolyte	Zn(OTF)$_2$-MeOH	Zn(OTF)$_2$-NAF	Zn(OTF)$_2$-NAF
Energy (Ha)	−115.6	−2240	−2356

Table S2 Ionic conductivities of different electrolytes.

Electrolyte	Zn(OTF)$_2$-H_2O	Zn(OTF)$_2$-MeOH	Zn(OTF)$_2$-NAF
σ (S cm^{-1})	7.89×10^{-3}	9×10^{-3}	1.22×10^{-2}

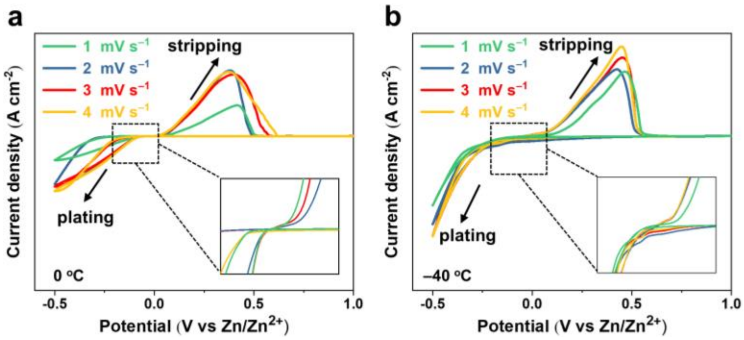

Fig. S5 Cyclic voltammetry curves of Zn||Cu cell at different scan rates. (a) $Zn(OTF)_2$-H_2O and (b) $Zn(OTF)_2$-NAF electrolyte.

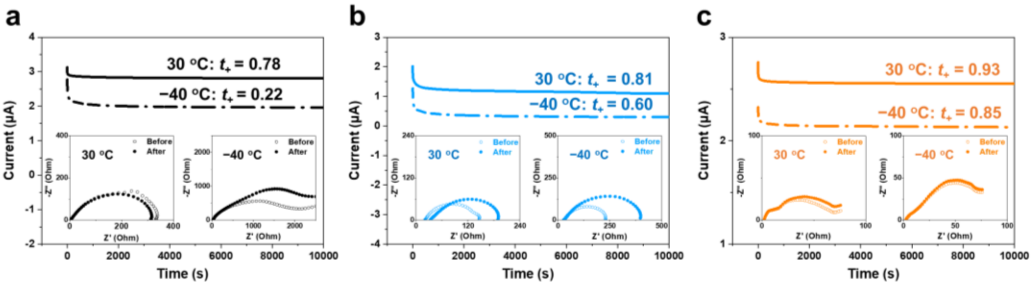

Fig. S6 Zn ion transfer number analysis in (a) $Zn(OTF)_2$-H_2O, (b) $Zn(OTF)_2$-MeOH and (c) $Zn(OTF)_2$-NAF electrolytes.

Notes to Fig. S6: The Zn^{2+} ion transfer numbers (t_+) of the electrolytes were determined *via* a commonly applied potentiates polarization technique. A voltage of 10 mV (ΔV) was applied to a Zn||Zn cell for 2 h to obtain an initial current I_0 and cut-off current I_{ss}. EIS testing was applied before and after the polarization to obtain the initial cell impedance (R_0), and the steady state cell impedance (R_{SS}). t_+ was calculated using the following equation:

$$t_+ = \frac{I_{SS}(\Delta V - I_0 R_0)}{I_0(\Delta V - I_{SS} R_{SS})}$$

In Fig. S6a, the migration numbers of Zn^{2+} ions are 0.78 and 0.22 (30 and −40 °C) in $Zn(OTF)_2$-H_2O electrolyte, indicating an unstable Zn^{2+} ions nucleation and a high reduction potential at anode/electrolyte interface (Fig. 1f). Similarly, without the regulation by NAF-nanofilm (Fig. S6b), the Zn^{2+} transport kinetics is slower in $Zn(OTF)_2$-MeOH electrolyte (−40 °C). For $Zn(OTF)_2$-NAF electrolyte, the migration numbers of Zn^{2+} ions is 0.85 even at −40 °C, proving the lower Zn^{2+} ions nucleation barrier and rapid ions transport. Compared to $Zn(OTF)_2$-H_2O electrolyte, the higher Zn^{2+} ion migration numbers and lower nucleation energies in $Zn(OTF)_2$-NAF electrolyte achieving thermodynamically stable anode.

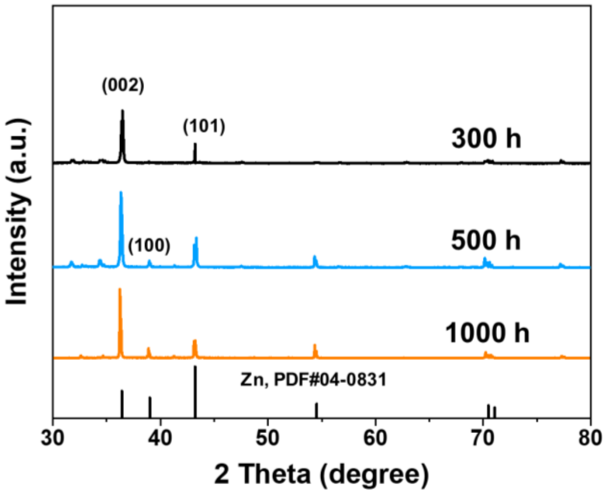

Fig. S7 XRD patterns of the Zn||Cu cell after Zn^{2+} plating/stripping in $Zn(OTF)_2$-NAF electrolyte.

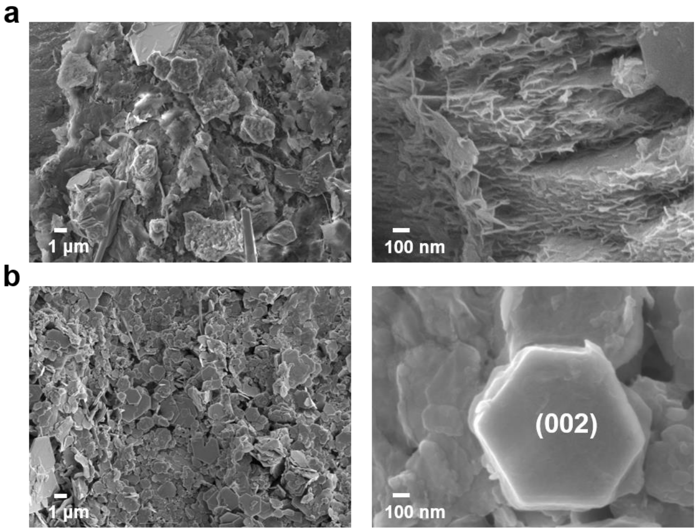

Fig. S8 SEM images of Zn^{2+} plating/stripping evolution after 200 h in (a) $Zn(OTF)_2$-H_2O and (b) $Zn(OTF)_2$-NAF electrolytes.

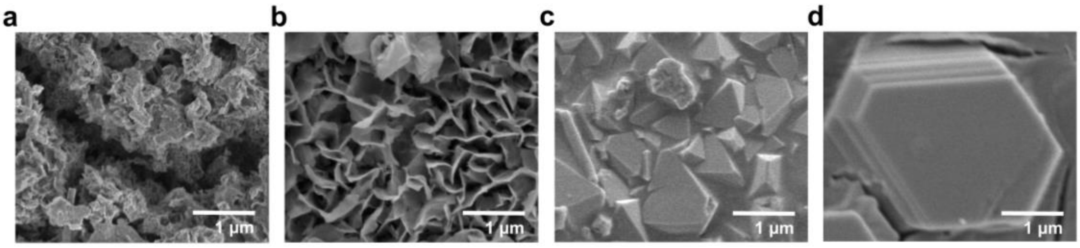

Fig. S9 The Zn^{2+} plating/stripping after 100 h at 5 mA cm^{-2} and 30 °C in: (a) 1 M $Zn(OTF)_2$-H_2O, (b) 2 M $Zn(OTF)_2$-H_2O, (c) 1 M $Zn(OTF)_2$-MeOH, and (d) 1 M $Zn(OTF)_2$-NAF electrolytes.

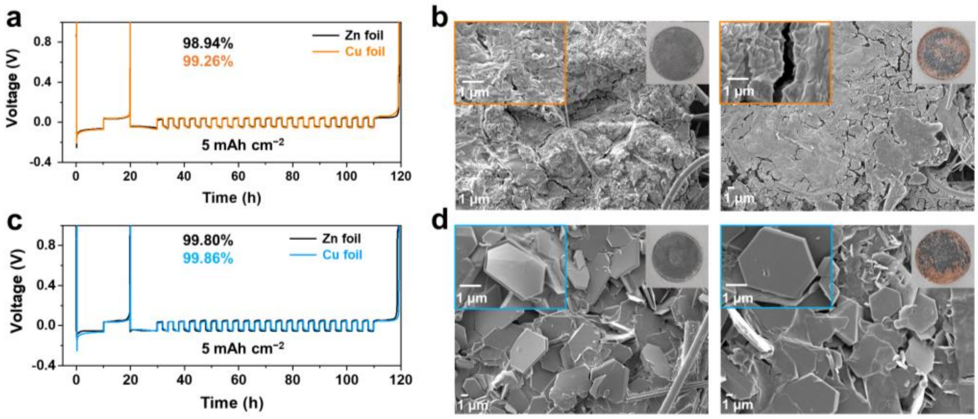

Fig. S10 The plating/stripping efficiency and corresponding morphology of different substrates in (a, b) $Zn(OTF)_2$-H_2O and (c, b) $Zn(OTF)_2$-NAF electrolytes. The insets are the optical images of the substrates.

Notes to Fig. S10: For $Zn(OTF)_2$-H_2O electrolyte, the plating/stripping efficiency of Cu/Zn foil are 98.54 and 99.26%, respectively (Fig. S10a), indicating that different substrates do not obviously affect the subsequent plating/stripping process. The nucleation and growth of deposited-Zn^{2+} on different substrates are disordered (Fig. S10b). Besides, the ruptured anode will further intensify parasitic reactions and hydrogen production. The plating/stripping efficiency of Cu/Zn foil increase to 99.80 and 99.86% in $Zn(OTF)_2$-NAF electrolytes (Fig. S10c), with a stable (002) crystal growth (Fig. S10d).

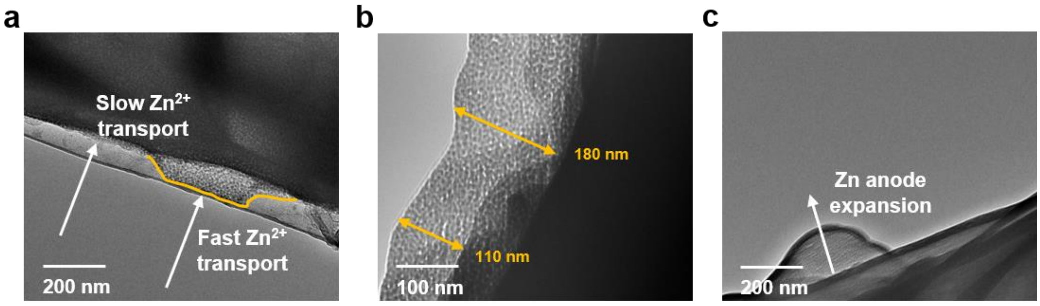

Fig. S11 TEM images of Zn deposited after 0.1 h at 5 mA cm^{-2} in $Zn(OTF)_2$-H_2O electrolyte at 30 °C. (a) Uneven Zn^{2+} plating. (b) The thickness of SEI. (c) Obvious interface expansion.

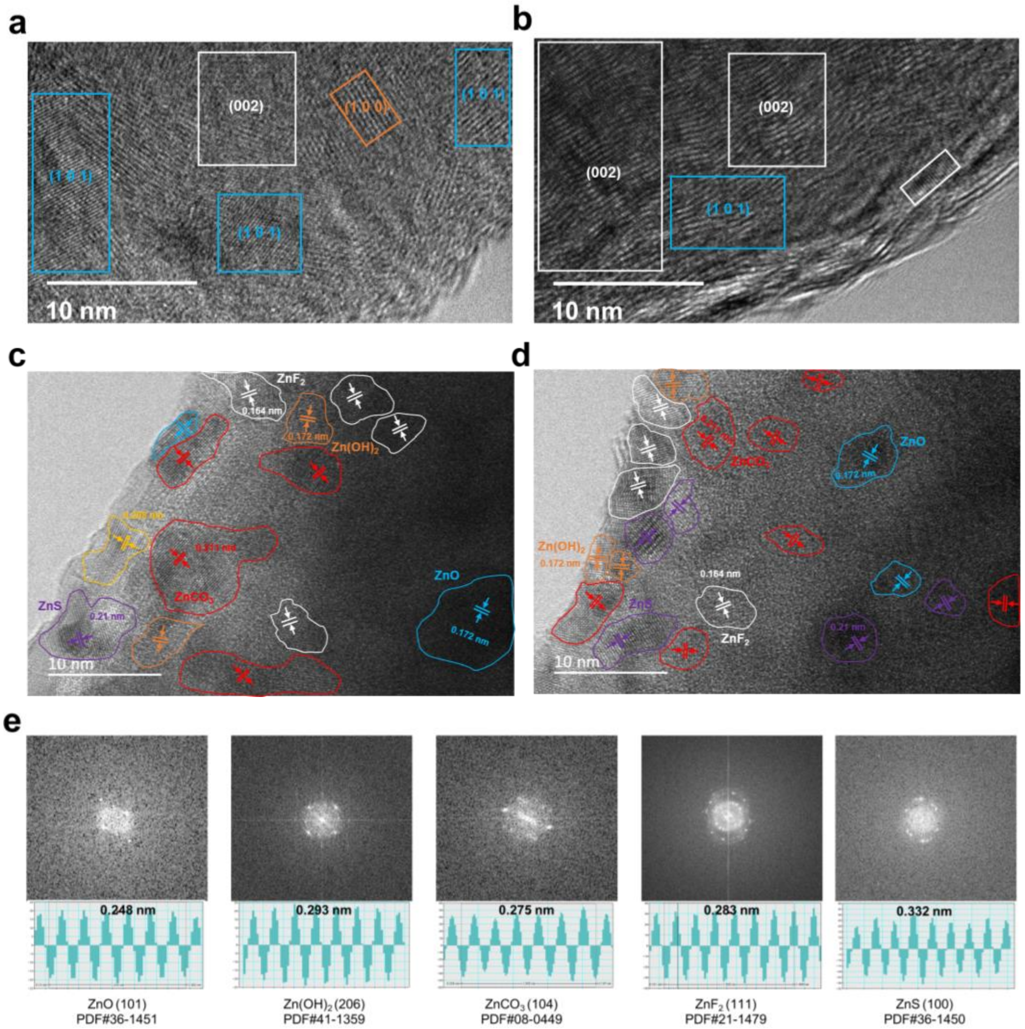

Fig. S12 HRTEM analysis of crystal growth and SEI composition in different electrolytes at 10 mA cm^{-2}. The crystal growth in (a) Zn(OTF)$_2$-H$_2$O and (b) Zn(OTF)$_2$-NAF electrolytes. Specific chemical components in: (c) Zn(OTF)$_2$-H$_2$O and (d) Zn(OTF)$_2$-NAF electrolytes. (e) The corresponding IFFT images of SEI components.

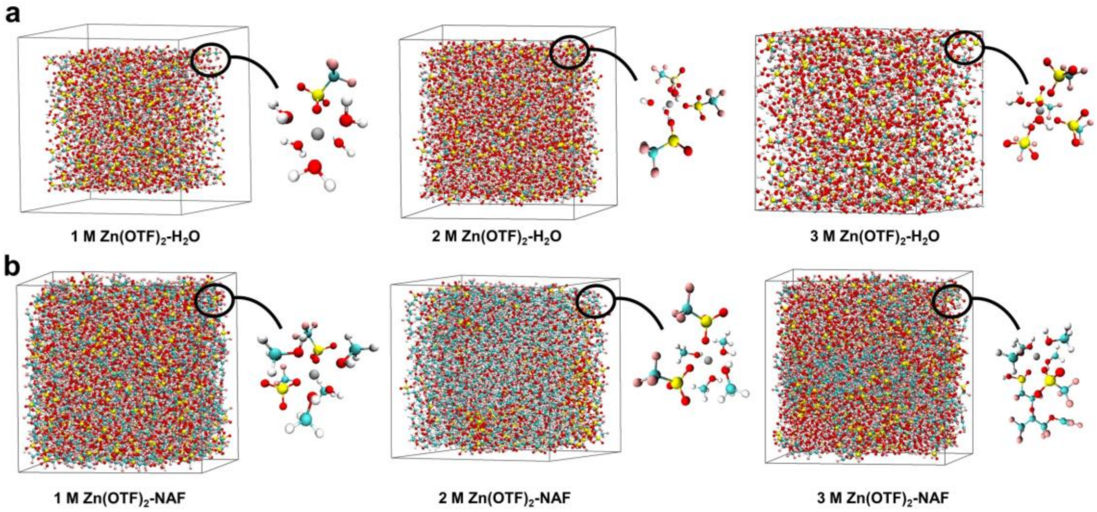

Fig. S13 Schematic diagrams of kinetic simulation processes and solvated structures of Zn^{2+} ions for different concentrations of $Zn(OTF)_2$. (a) 1 to 3 M $Zn(OTF)_2$ in aqueous electrolyte and (b) 1 to 3 M $Zn(OTF)_2$ in $Zn(OTF)_2$-NAF electrolyte.

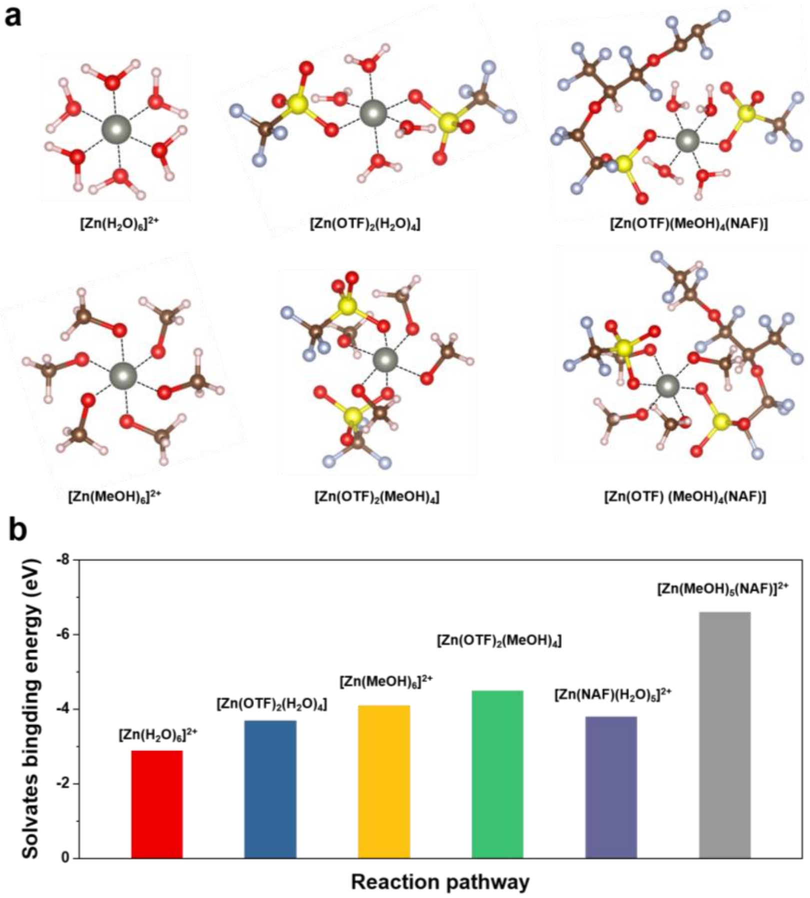

Fig. S14 (a) Coordination structure diagrams of Zn^{2+} ions in different electrolytes. (b) Binding energy of Zn^{2+} coordination structure.

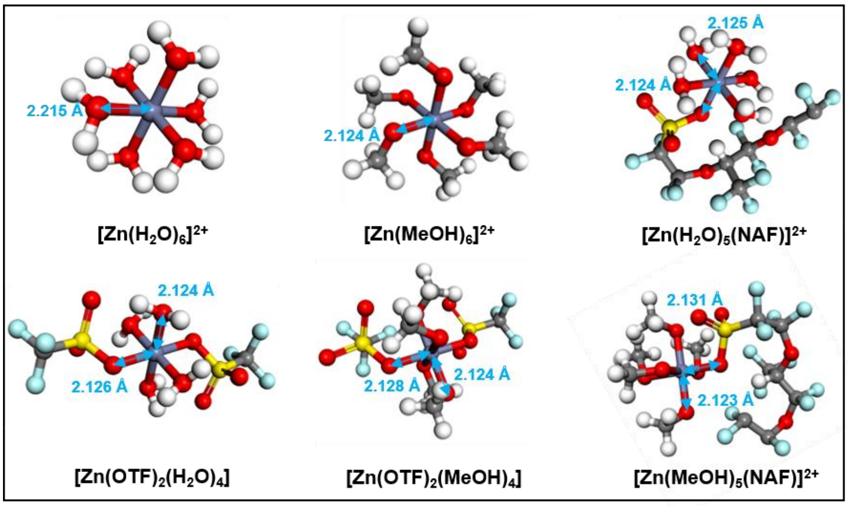

Fig. S15 Coordination distances between different ligands and Zn^{2+} ions.

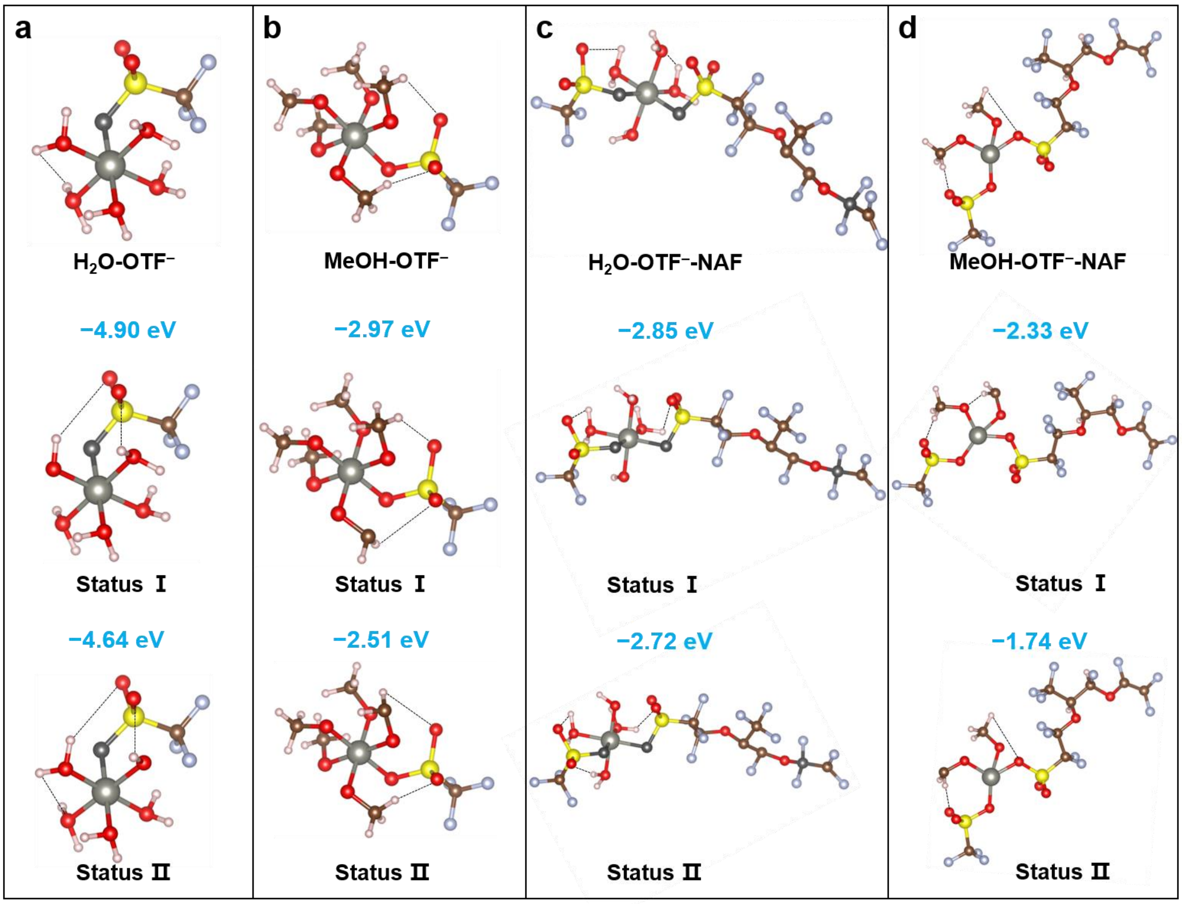

Fig. S16 Deprotonation energy computed *via* DFT for (a) $[Zn(H_2O)_5OTF]^+$, (b) $[Zn(MeOH)_5OTF]^+$, (c) $[Zn(H_2O)_4(NAF)OTF]^+$, and (d) $[Zn(MeOH)_4OTF]^+$.

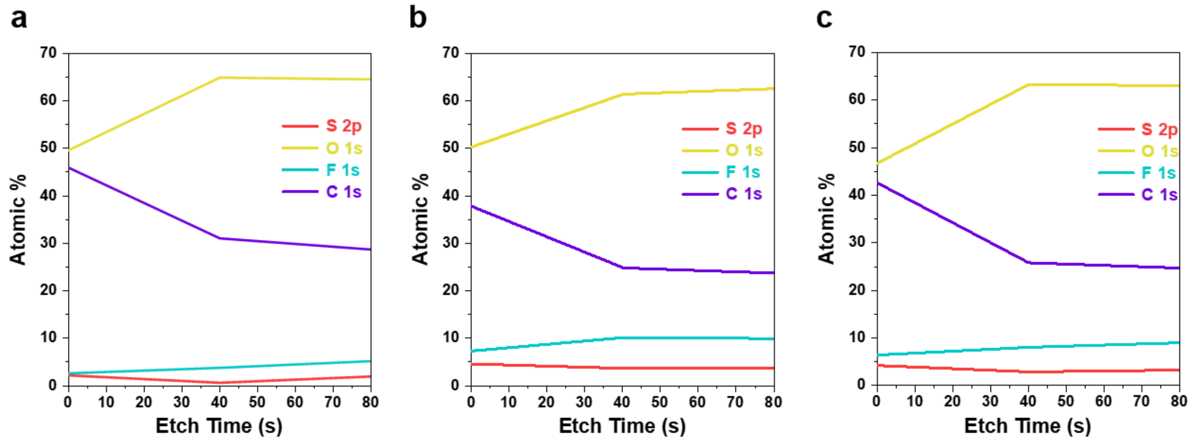

Fig. S17 Proportional distribution of chemical element content after deposition in: (a) $Zn(OTF)_2$-H_2O, (b) $Zn(OTF)_2$-MeOH, and (c) $Zn(OTF)_2$-NAF electrolytes.

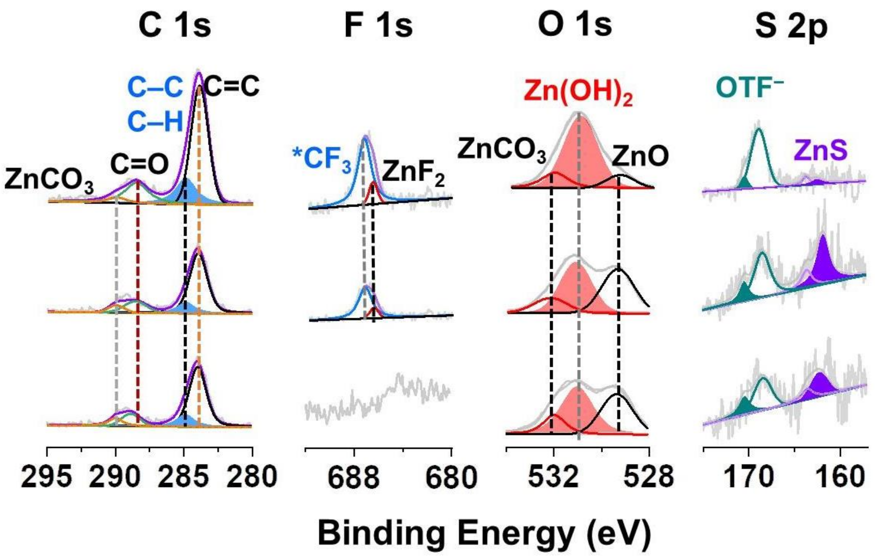

Fig. S18 *In-depth* XPS spectra analysis of SEI in $Zn(OTF)_2$-MeOH electrolyte.

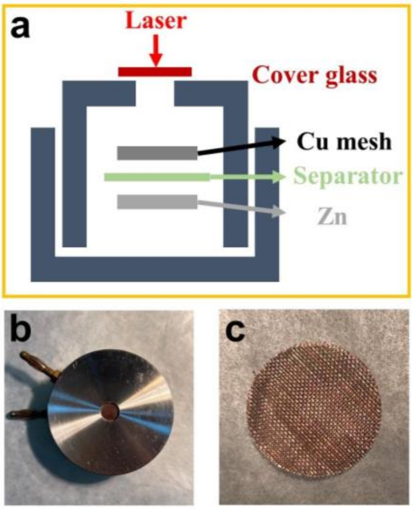

Fig. S19 (a) Schematic diagram of *in-situ* Raman cell (b) *in situ* cell, and (c) Cu mesh.

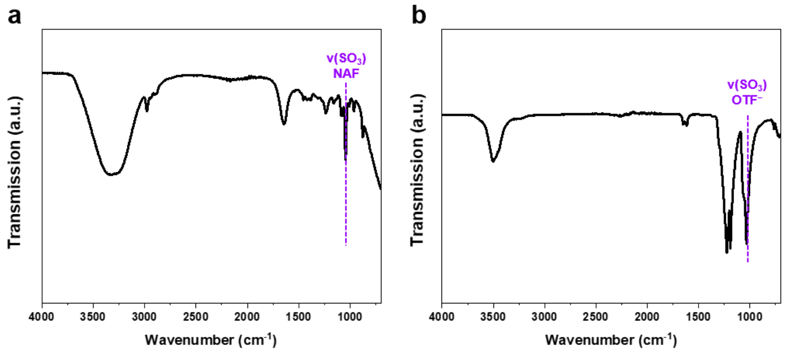

Fig. S20 FTIR detection results of electrolyte components: (a) Nafion solution and (b) $Zn(OTF)_2$.

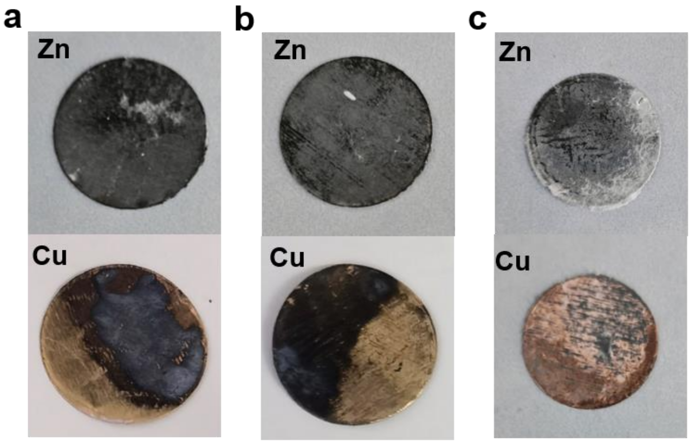

Fig. S21 Corrosion of Zn and Cu after 100 h cycling at 10 mA cm^{-2} and 30 ^{o}C in (a) $Zn(OTF)_2$-H_2O, (b) $Zn(OTF)_2$-MeOH, and (c) $Zn(OTF)_2$-NAF electrolytes.

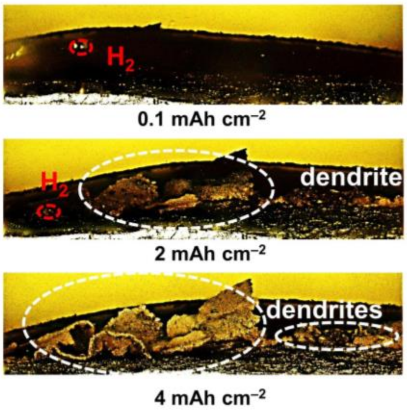

Fig. S22 *In-situ* DOF microscope plating images at −40 °C in Zn(OTF)₂-MeOH electrolyte.

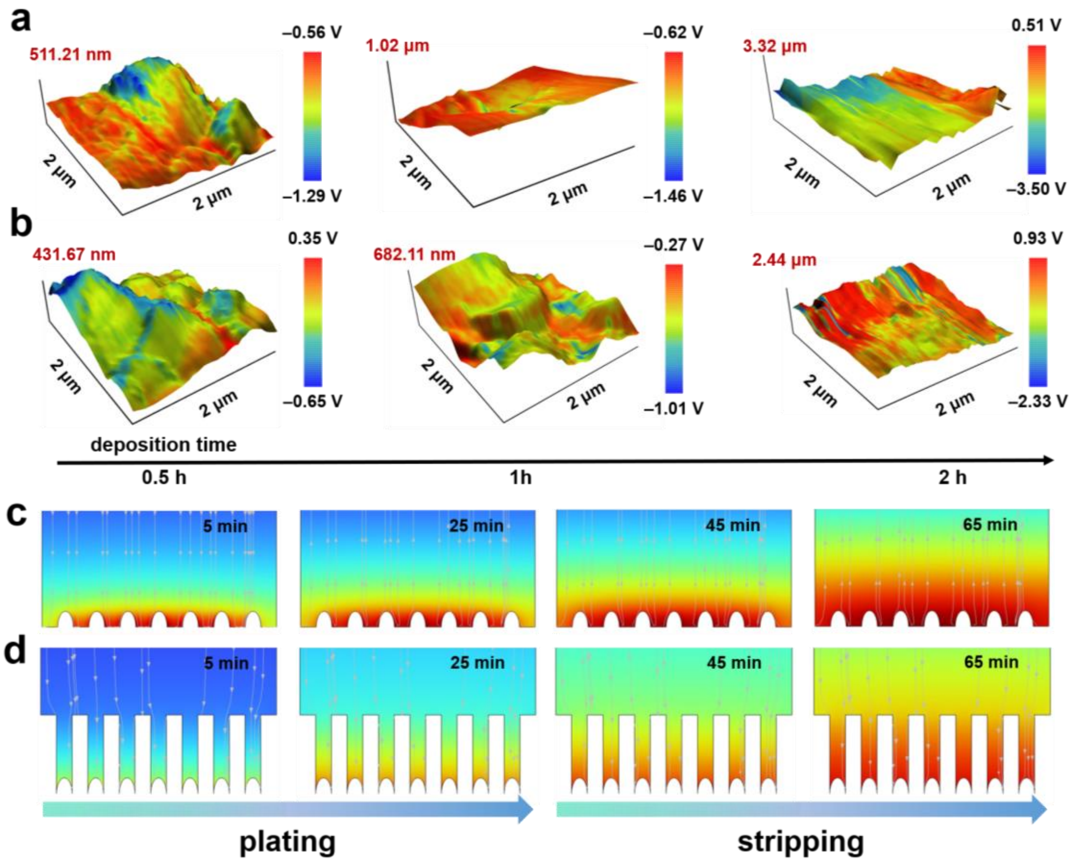

Fig. S23 The surface potential and morphology evolution of Zn anodes in Zn||Zn cells after cycling (the current density was 2 mA cm^{-2}) using (a) Zn(OTF)$_2$-H$_2$O and (b) Zn(OTF)$_2$-MeOH electrolytes. Schematic diagram of COMSOL physical field simulation for (c) Zn(OTF)$_2$-H$_2$O and (d) Zn(OTF)$_2$-NAF electrolytes.

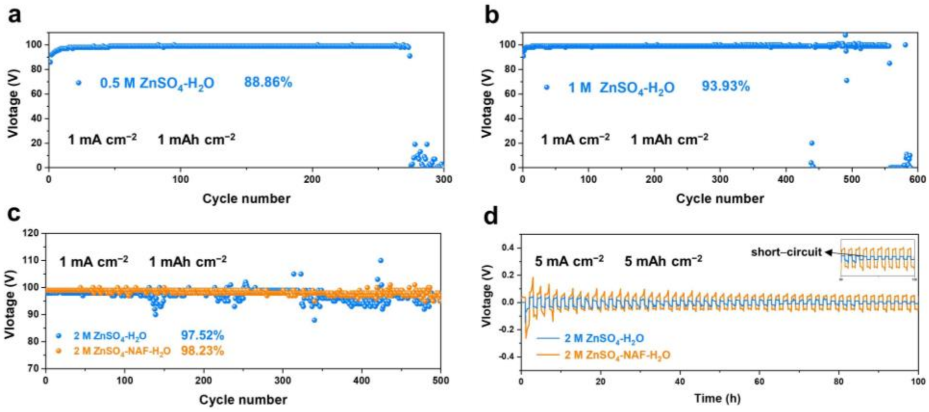

Fig. S24 Deposition Coulombic efficiency (CE) of Zn||Cu cells at 30 ^{o}C in (a) 0.5 M, (b) 1 M, and (c) 2 M $ZnSO_4$-H_2O electrolytes. (d) Overpotential test of Zn||Zn cells.

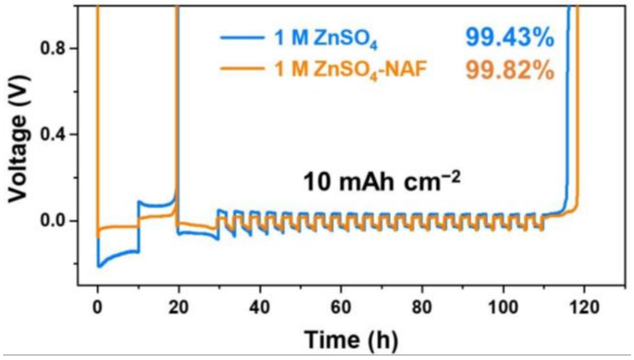

Fig. S25 Voltage-time curves of Zn||Cu cells in $ZnSO_4$ electrolytes at 30 ^{o}C.

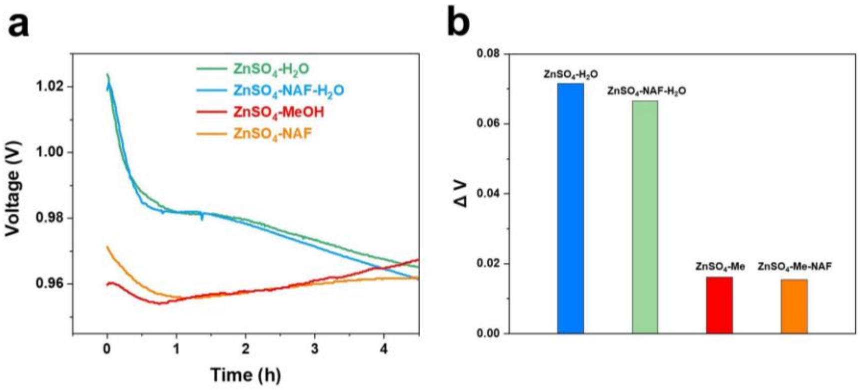

Fig. S26 Voltage-drop of Zn||Cu cells during deposition process at −40 ^{o}C: (a) Voltage-time curves and (b) Self-discharge levels.

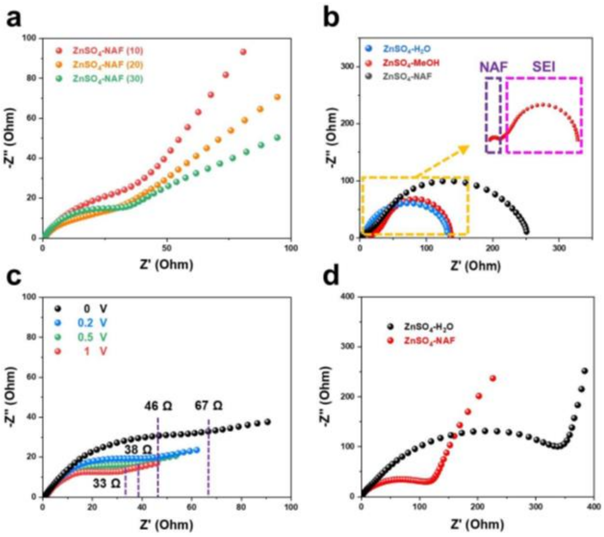

Fig. S27 (a) EIS test during the first discharge process of Zn||Zn cells in $ZnSO_4$-NAF electrolyte. (b) EIS of Zn||Zn cells with various electrolytes after 5 cycles. (c) *Ex-situ* EIS of Zn||Cu cells during discharging process in $ZnSO_4$-NAF electrolyte. (d) EIS of Zn||MnO_2 cells after 100 cycles.

Table S3 Assignment of XPS signals.

Source	Species	Binding Energy (eV)
C 1s	CF species	290[13]
	C−O−C	286.2[13]
	C−C/C−H	285.3[13]
	C=C	284.6[14]
	$ZnCO_3$	288.6[15]
F 1s	−CF*	689.4[13]
	ZnF_2	684.9[15]
S 2p	SO_3	170.5 (S 2p 1/2) 169.3 (S 2p 3/2)[16]
	ZnS	163.6 (S 2p 1/2) 162.4 (S 2p 3/2)[15]

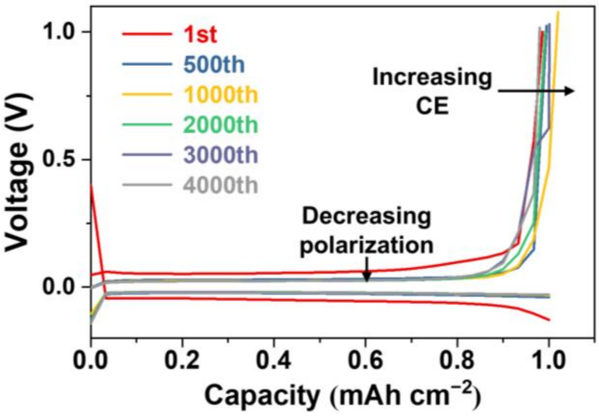

Fig. S28 The corresponding charge-discharge curves of Zn||Cu cell in Zn(OTF)$_2$-NAF electrolytes at selected cycles.

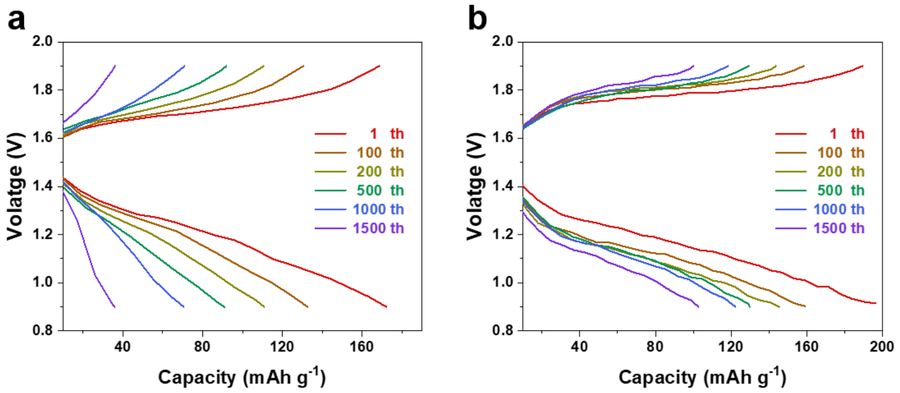

Fig. S29 GCD curves of Zn||MnO$_2$ cells during different cycles using (a) Zn(OTF)$_2$-H$_2$O and (b) Zn(OTF)$_2$-NAF electrolytes.

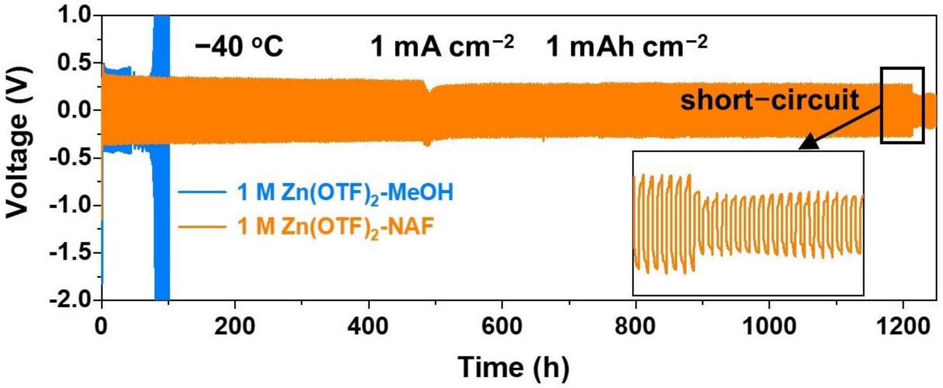

Fig. S30 GCD curves of Zn||MnO$_2$ cells during different cycles using (a) Zn(OTF)$_2$-H$_2$O and (b) Zn(OTF)$_2$-NAF electrolytes.

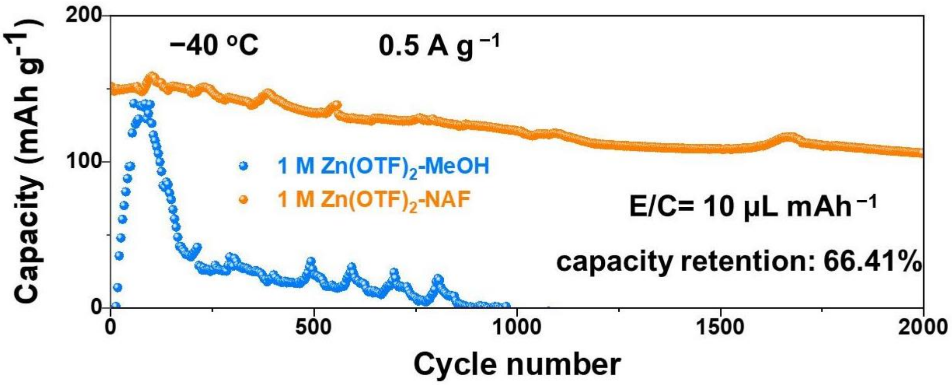

Fig. S31 GCD curves of Zn||MnO$_2$ cells during different cycles using (a) Zn(OTF)$_2$-H$_2$O and (b) Zn(OTF)$_2$-NAF electrolytes.

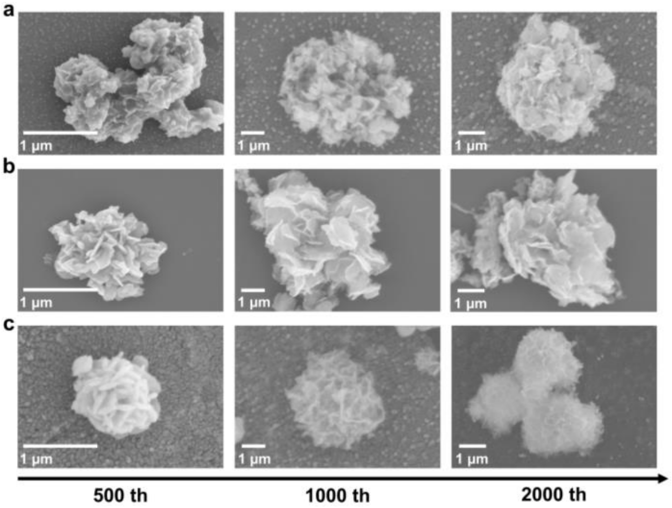

Fig. S32 SEM images of α-MnO$_2$ cathode structure after different cycles in (a) Zn(OTF)$_2$-H$_2$O, (b) Zn(OTF)$_2$-MeOH and (c) Zn(OTF)$_2$-NAF electrolytes at 30 °C.

Notes to Fig. S32: The structure of α-MnO$_2$ in various electrolytes shows significant differences after cycling. Affected by the insertion/extraction of hydrated Zn^{2+} ions, the structure of α-MnO$_2$ begins to collapse after the 500th cycle in Zn(OTF)$_2$-H$_2$O electrolyte. The nanoflower gradually pulverizes and further deteriorates after the 2000 th cycle (Fig. S32a). Similarly, without the protection of NAF-film, the structure of α-MnO$_2$ in Zn(OTF)$_2$-MeOH electrolyte is also disrupted (Fig. S32b). Notably, the morphology of MnO$_2$ cathode maintains a complete nanoflower structure after 2000 cycles in Zn(OTF)$_2$-NAF electrolyte, confirming high stability of the Zn||MnO$_2$ cell (Fig. S32c).

Table S4 A comparison of the performances of Zn||Zn cells using different electrolytes.

Electrolyte	Current density (mA cm^{-2})	Cycle capacity (mAh cm^{-2})	Cycle life (h)	Refs.
Zn(OTF)$_2$-NAF	5	5	7000	This work
Azi@ZnSO$_4$	1	1	4000	17
TMP-40	1	5	500	18
PG50	0.5	0.5	3500	19
ZnSO$_4$+Suc	2	2	3500	20
PDADMAC	5	5	2300	21
SA-Zn	0.5	0.5	900	22
LiBOB	5	1	3700	23
Gel/SA	0.1	0.1	1600	24
ZBFD	1	10	3000	25
CoSA/C	1	1	2000	26
Sb$_2$O$_3$@Zn	1	0.5	2800	27
ZIG	1	0.5	900	28
PZIL	1	1	1000	29
ZnOAc$_{1.2}$Cl$_{1.8}$	5	1	1000	30
Zn(PS)$_2$	1	1	1200	31
C-PAMCS	5	5	2700	32
70SL	2	8	1600	33
SSE-EC	0.1	0.1	6000	34
TMP-DMC	1	2	5000	35

Table S5 A comparison of the performances of Zn||MnO_2cells using different electrolytes.

Electrolyte	Current (A g^{-2})	Cycle life (h)	Refs.
Zn$(OTF)_2$-NAF	1	3000	This work
MZn-60	1	500	36
Zn_5Cu	5	600	37
$ZnSO_4$-H_2O-NMP	0.5	100	38
TiN/TiO_2	0.1	600	39
KL	0.5	500	40
Zn$(TFSI)_2$-TFEP@MOF	10	600	41
$ZnBr_2$+PEG300	1	1000	42
PZAS	1	500	43
OSGE	1	2000	44
CZn	1	1000	45
3D-LC/3D-RFGC@Zn	2	500	46

References

1. B. Jia, W. Chen, J. Luo, Z. Yang, L. Li, L. Guo, *Adv. Mater.*, 2020, **32**, 1906582.
2. Z. Fang, Y. Yang, T. Zheng, N. Wang, C. Wang, X. Dong, Y. Wang, Y. Xia, *Energy Storage Mater.*, 2021, **42**, 477−483.
3. Y. Deng, S. Dong, Z. Li, H. Jiang, X. Zhang, X. Ji, *Small Methods*, 2018, **2**, 1700332;
4. X. Wang, C. Gao, J. Low, K. Mao, D. Duan, S. Chen, R. Ye, Y. Qiu, J. Ma, X. Zheng, R. Long, X. Wu, L. Song, J. Zhu, Y. Xiong, *Sci. Bull.*, 2021, **66**, 1296−1304.
5. G. Kresse, J. Furthmüller, *Comput. Mater. Sci.*, 1996, **6**, 15−50.
6. G. Kresse, D. Joubert, *Phys. Rev. B*, 1999, **59**, 1758−1775.
7. P. E. Blöchl, *Phys. Rev. B*, 1994, **50**, 17953−17979.
8. J. P. Perdew, K. Burke, M. Ernzerhof, *Phys. Rev. Lett.,* 1996, **77**, 3865−3868.
9. M. Methfessel, A. T. Paxton, *Phys. Rev. B*, 1989, **40**, 3616−3621.
10. J. D. Pack, H. J. Monkhorst, *Phys. Rev. B*, 1977, **16**, 1748−1749.
11. K. Lee, É. D. Murray, L. Kong, B. I. Lundqvist, D. C. Langreth, *Phys. Rev. B,* 2010, **82**, 081101.
12. J. Manigrasso, I. Chillón, V. Genna, P. Vidossich, S. Somarowthu, A. M. Pyle, M. De Vivo, M. Marcia, *Nat. Commun.*, 2022, **13**, 1.
13. Y. Wang, B. Liang, J. Zhu, G. Li, Q. Li, R. Ye, J. Fan, C. Zhi, *Angew. Chem. Int. Ed.,* 2023, **62**, e202302583.
14. Y. Yang, S. Guo, Y. Pan, B. Lu, S. Liang, J. Zhou, *Energy Environ. Sci.,* 2023, **16**, 2358−2367.
15. L. Cao, D. Li, T. Pollard, T. Deng, B. Zhang, C. Yang, L. Chen, J. Vatamanu, E. Hu, M. J. Hourwitz, L. Ma, M. Ding, Q. Li, S. Hou, K. Gaskell, J. T. Fourkas, X. Q. Yang, K. Xu, O. Borodin, C. Wang, *Nat. Nanotechnol.,* 2021, **16**, 902−910.
16. Y. Wang, T. Wang, D. Dong, J. Xie, Y. Guan, Y. Huang, J. Fan, Y. C. Lu, *Matter,* 2022, **5**, 162−179.
17. X. Bai, Y. Nan, K. Yang, B. Deng, J. Shao, W. Hu, X. Pu, *Adv. Funct. Mater.,* 2023, **33**, 2307595.
18. W. Wang, S. Chen, X. Liao, R. Huang, F. Wang, J. Chen, Y. Wang, F. Wang, H. Wang, *Nat. Commun.,* 2023, **14**, 5443.

19. J. Li, S. Zhou, Y. Chen, X. Meng, A. Azizi, Q. He, H. Li, L. Chen, C. Han, A. Pan, *Adv. Funct. Mater.,* 2023, **33**, 2307201.

20. L. Zhou, R. Yang, S. Xu, X. Lei, Y. Zheng, J. Wen, F. Zhang, Y. Tang, *Angew. Chem. Int. Ed.,* 2023, **62**, e202307880.

21. L. Chen, Y. Han, Z. Wang, Q. Li, J. Zhang, *Adv. Funct. Mater.,* 2023, **33**, 2308023.

22. H. Dong, X. Hu, R. Liu, M. Ouyang, H. He, T. Wang, X. Gao, Y. Dai, W. Zhang, Y. Liu, Y. Zhou, D. J. L. Brett, I. P. Parkin, P. R. Shearing, G. He, *Angew. Chem. Int. Ed.*, 2023, **62**, e202311268.

23. Z. Zhang, Y. Zhang, M. Ye, Z. Wen, Y. Tang, X. Liu, C. C. Li, *Angew. Chem. Int. Ed.,* 2023, **62**, e202311032.

24. C. Tian, J. Wang, R. Sun, T. Ali, H. Wang, B. B. Xie, Y. Zhong, Y. Hu, *Angew. Chem. Int. Ed.,* 2023, **62**, e202310970.

25. C. Meng, W. D. He, H. Tan, X. L. Wu, H. Liu, J. J. Wang, *Energy Environ. Sci.,* 2023, **16**, 3587-3599.

26. W. Fan, P. Li, J. Shi, J. Chen, W. Tian, H. Wang, J. Wu, G. Yu, *Adv. Mater.,* 2024, **36**, 2307219.

27. P. Xiao, Y. Wu, K. Liu, X. Feng, J. Liang, Y. Zhao, C. Wang, X. Xu, T. Zhai, H. Li, *Angew. Chem. Int. Ed.,* 2023, **62**, e202309765

28. Y. Wang, Q. Li, H. Hong, S. Yang, R. Zhang, X. Wang, X. Jin, B. Xiong, S. Bai, C. Zhi, *Nat. Commun.,* 2023, **14**, 3890.

29. Meng, Z., Jiao, Y., Wu, P., *Angew. Chem. Int. Ed.,* 2023, **62**, e202307271.

30. X. Lu, Z. Liu, A. Amardeep, Z. Wu, L. Tao, K. Qu, H. Sun, Y. Liu, J. Liu, *Angew. Chem. Int. Ed.*, 2023, **62**, e202307475.

31. S. Chen, D. Ji, Q. Chen, J. Ma, S. Hou, J. Zhang, *Nat. Commun.,* 2023**, 14**, 3526.

32. Q. Liu, Z. Yu, Q. Zhuang, J. K. Kim, F. Kang, B. Zhang, *Adv. Mater.,* 2023, **35**, 2300498.

33. C. Li, R. Kingsbury, A. S. Thind, A. Shyamsunder, T. T. Fister, R. F. Klie, K. A. Persson, L. F. Nazar, *Nat. Commun.,* 2023, **14**, 3067.

34. B. Qiu, K. Liang, W. Huang, G. Zhang, C. He, P. Zhang, H. Mi, *Adv. Energy Mater.,* 2023, **13**, 2301193.

35. A. Naveed, H. Yang, Y. Shao, J. Yang, N. Yanna, J. Liu, S. Shi, L. Zhang, A. Ye, B. He, J.

Wang, *Adv. Mater.,* 2019, **31**, 1900668.

36. N. Zhang, S. Huang, Z. Yuan, J. Zhu, Z. Zhao, Z. Niu, *Angew. Chem. Int. Ed.,* 2021, **60**, 2861.
37. H. Tian, G. Feng, Q. Wang, *Nat Commun.,* 2022, **13**, 7922.
38. D. Wang, D. Lv, H. Liu, S. Zhang, C. Wang, C. Wang, J. Yang, Y. Qian, *Angew. Chem. Int. Ed.,* 2022, **61**, e202212839.
39. S. Chen, R. Lan, J. Humphreys, S. Tao, *Energy Storage Mater.,* 2020, **28**, 205−215.
40. Y. Pan, Z. Liu, S. Liu, L. Qin, Y. Yang, M. Zhou, Y. Sun, X. Cao, S. Liang, G. Fang, *Adv. Energy Mater.,* 2023, **13**, 2203766.
41. L. Cao, D. Li, T. Deng, Q. Li, C. Wang, *Angew. Chem. Int. Ed.,* 2020, **59**, 19292.
42. S. Jin, J. Yin, X. Gao, A. Sharma, P. Chen, S. Hong, Q. Zhao, J. Zheng, Y. Deng, Y. L. Joo, L. A. Archer, *Nat. Commun.,* 2022, **13**, 2283.
43. Y. Yuan, J. Yang, Z. Liu, R. Tan, M. Chuai, J. Sun, Y. Xu, X. Zheng, M. Wang, T. Ahmad, N. Chen, Z. Zhu, K. Li, W. Chen, *Adv. Energy Mater.,* 2022, **12**, 2103705.
44. S. Chen, P. Sun, J. Humphreys, P. Zou, M. Zhang, G. Jeerh, S. Tao, *Energy Storage Mater.* 2021, **42**, 240−251.
45. Z. Zhao, J. Zhao, Z. Hu, J. Li, J. Li, Y. Zhang, C. Wang, G. Cui, *Energy Environ. Sci.,* 2019, **12**, 1938−1949.
46. Y. Mu, Z. Li, B. k. Wu, H. Huang, F. Wu, Y. Chu, L. Zou, M. Yang, J. He, L. Ye, M. Han, T. Zhao, L. Zeng, *Nat. Commun.,* 2023, **14**, 4205.